
SiBBInGS: Similarity-driven Building-Block Inference using Graphs across States

Noga Mudrik

Biomedical Engineering, Kavli NDI, CIS
The Johns Hopkins University
Baltimore, MD, 21218
nmudrik1@jhu.edu

Gal Mishne

Halıcıoğlu Data Science Institute
UCSD
San Diego, CA, 92093
gmishne@ucsd.edu

Adam S. Charles

Biomedical Engineering, Kavli NDI, CIS
The Johns Hopkins University
Baltimore, MD, 21218
adamsc@jhu.edu

Abstract

Interpretable methods for extracting meaningful building blocks (BBs) underlying multi-dimensional time series are vital for discovering valuable insights in complex systems. Existing techniques, however, encounter limitations that restrict their applicability to real-world systems, like reliance on orthogonality assumptions, inadequate incorporation of inter- and intra-state variability, and incapability to handle sessions of varying duration. Here, we present a framework for Similarity-driven Building Block Inference using Graphs across States (SiBBInGS). SiBBInGS employs a graph-based dictionary learning approach for BB discovery, simultaneously considers both inter- and intra-state relationships in the data, can extract non-orthogonal components, and allows for variations in session counts and duration across states. Additionally, SiBBInGS allows for cross-state variations in BB structure and per-trial temporal variability, can identify state-specific vs state-invariant BBs, and offers both supervised and data-driven approaches for controlling the level of BB similarity between states. We demonstrate SiBBInGS on synthetic and real-world data to highlight its ability to provide insights into the underlying mechanisms of complex phenomena and its applicability to data in various fields.

1 Introduction

The analysis of high-dimensional time series data is increasingly important across various scientific disciplines, ranging from neuroscience [31, 2, 39] to social sciences [30, 20] to genetics [5, 52]. However, high-dimensional time series present a daunting challenge in terms of comprehensibility as they often stem from a multitude of intricate factors, both observed and unobserved.

In particular, data acquisition in many domains involves gathering observations under diverse states, including controlled interventions, environmental shifts, and potential hidden factors internal to the observed system [7, 23]. Thus, latent factors can lead to variability in how these systems are observed within and between states, emphasizing the need for new methodologies that can capture the temporal dynamics effectively while accounting for structured variability. For example, in neuroimaging, identifying latent structures and their activity across different tasks and individuals provides critical insights into the mechanisms of neurological disorders and brain function [49, 63].

Current analysis methods, however, often struggle to capture the complex inter- and intra-state variability critical for fully understanding such multi-view data.

Moreover, integrating data from multiple observations within the same state into a coherent representation is often complicated by different session duration, missing samples, or varying sampling rates [24, 11, 18], and the common practice of trial averaging can obscure important patterns presented in individual trials. Hence, accounting for this intra-state variability is crucial for accurately capturing the full spectrum of dynamics underlying the data. A promising approach to facilitate effective analyses of multi-state high-dimensional data is through the identification of fundamental building blocks (BBs) shared across trials and states. BBs can represent, e.g., neural ensembles in the brain, social networks among individuals, or genetic pathways in cells, and their corresponding time-traces (i.e., activity patterns over time) represent important system dynamics. By offering a shared basis, identifying similar BBs across states holds promise for enhancing, streamlining, and providing a more interpretable representation of the underlying processes driving the observed dynamics. Cross-state BBs can further offer valuable insights into inter- and intra-state variability by examining how the temporal activity of each BB differs within and between states. However, while these BBs may represent significant unseen effects, their identification can pose a challenge due to their obscurity. This challenge is further compounded by the potential for cross-state variations in their structure in addition to the aforementioned cross-trial temporal variability. For instance, in neuroscience, a BB representing a functional network is expected to present small variations in its connectivity or neuron membership across different conditions [40, 59].

We thus present SiBBInGS, a graph-driven framework for understanding high-dimensional multi-state time series by identifying sparse, interpretable latent BBs underlying the data. These BBs are inferred based on shared membership across sessions, and need not be orthogonal nor independent. Thus, SiBBInGS accounts for both within- and between-state variability and facilitates exploration of the latent organization of data across trials and states. Additionally, SiBBInGS enables the analysis of sessions with different time duration, sampling rates, and different number of sessions within each state, and supports both supervised and data-driven versions for defining similarities between states. We demonstrate that these properties have the potential to provide critical insights into the underlying mechanisms of complex systems via both simulated data and real-world examples, including Google Trends data and multi-unit neural recordings.

2 Background and related Work

Data decomposition. Conventional 2D methods for identifying BBs underlying time-series often rely on Singular Value Decomposition (SVD) [32], Principal Components Analysis (PCA) [28], Independent Components Analysis (ICA) [29], or Non-negative Matrix Factorization (NMF) [34], which prioritize identifying components based on maximum variability or independence. Newer methods, such as Dynamic Mode Decomposition (DMD) [50], further model the temporal dynamics more explicitly as dynamical systems. However, the design of these methods for 2D analysis makes their application to multi-state and multi-session data challenging. Tensor decomposition (e.g., PARAFAC/TCA [26, 60, 38]) and higher-order matrix decomposition (e.g., HOSVD [17]) offer alternatives to traditional 2D methods by considering states or trials as additional dimensions, thus accounting for higher-order tensors (high dimensional arrays).

All these methods, however, are inherently data-driven and do not use additional state or trial meta-information. Targeted dimensionality reduction (TDR) [36] and model-based TDR (mTDR) [36, 3, 4] directly regress rank-1 (for TDR) or low-rank (for mTDR) components that target task-relevant variables explicitly. More recently, nonlinear deep learning with transformers has also been applied to discover latent components [35]. The encoder-Interaction-Transformer model (EIT) [35] jointly models individual and collective dynamics via an individual module for each of several component dynamics and an interaction module capturing collective behavior through pairwise interactions. However, EIT relies on prior knowledge and the limited size of its final representation space restricts of the model’s representational capacity. In addition, it depends on labels for functional alignment, and potentially requires large-scale data to train the encoder-decoder models. Thus, its ability to extract meaningful relationships in data and to capture within-state variability might be limited.

More recent work complements the aforementioned techniques by incorporating auxiliary labels and temporal information while employing a contrastive optimization objective [51]. However,

CEBRA cannot function on sessions of different duration, is contingent upon the availability of sufficient training data for the neural networks, and produces a latent state that requires additional interpretation steps to connect to a neuronal-level mechanistic understanding.

Data decomposition on multiple data arrays. Some models aim to account for similar BBs across states. In the shared response model (SRM) [13], a multi-subject fMRI model is proposed where the same temporal activity applies to all individuals (states) who may have different spatial responses. However, SRM maintains the above-mentioned limiting orthonormality assumption and restricts spatial map changes to small variations. Multi-dataset low-rank matrix factorization [54] is another relevant technique. Yet, it assumes an identical shared structure across data sets and requires pre-alignment and pre-processing, which may not always be practical.

Fuzzy clustering [62]—and similarly the wavelet tensor fuzzy clustering scheme (WTFCS) [27]—allows data points to have varying degrees of membership in multiple clusters, overcoming the limitations of the orthogonality assumption. In the context of 3D tensor data, a multiview extension of fuzzy clustering [57] utilizes low-rank tensor regularization to jointly learn clustering assignments and low-rank tensor factors. However, this approach similarly cannot address varying trial duration or changing shapes across views.

The above approaches are all constrained in their capacity to dynamically capture the intricacies of multi-state multi-trial variability while simultaneously accommodating cross-state variations in the BB structures. Particularly, they are either restricted by an orthogonality assumption [17, 13], limited interpretability [17, 26], inability to handle trials of different duration [17, 26, 60, 36, 3, 4, 57, 27], or a need for detailed labels and sufficient training data [35, 51], cannot incorporate both within and between state variability [17, 26, 36, 50, 27], or cannot model cross-state variations in BB structure [17, 26, 60, 54, 50]. Consequently, there is a need for new approaches that can address these limitations and provide a more comprehensive framework for identifying and exploring the BB’s underlying high-dimensional multi-state data.

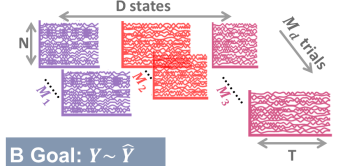
Sparse coding and re-weighted ℓ_1 filtering. Closer to our approach is dictionary learning (DL) [42, 41, 1]. DL is based on the idea that each data point can be reconstructed by a small number of vectors from a dictionary of feature vectors. Sparsity is achieved by decomposing the data under a sparsity-promoting regularization term (e.g., LASSO) and often provide more interpretable representations than, e.g., PCA [53]. DL often treats each individual data point as independent, ignoring similarities between individual points, e.g., ignoring temporal correlations between frames (i.e., the data points) in a video sequence. Recent models based on re-weighted ℓ_1 [8, 19] have been developed to modify the sparsity regularization terms to account for spatiotemporal similarities between data points [19, 12, 9, 64, 46, 37]. One of the most recent of these methods, Graph Filtered Time-trace estimation (GraFT) [10], was originally developed for demixing independent fluorescing components in calcium imaging recordings by learning a data-driven graph to correlate sparse decompositions across complex, non-Euclidean datasets. GraFT demonstrates that graph-based correlations can be effective in extracting meaningful components from large datasets, e.g., fluorescing neurons and dendrites from multi-photon microscopy data. However, GraFT is restricted to 2D data and only learns a graph along a single path of the data—in the original method in the pixel space. This limitation overlooks the possibility of meaningful structures existing in other ways, such as the variability between and within states.

3 The SiBBIInGS model

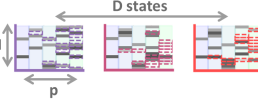
We propose a framework to identify interpretable BBs based on shared temporal activity within trials and shared activation patterns across trials and states. This framework serves as a foundation for understanding cross-trial and state variability, enabling deeper insights into how BBs differ across sessions both in terms of their structure and temporal dynamics. Unlike existing methods, SiBBIInGS clusters BB components based on temporal similarity, enabling the study of variability in multi-state high-dimensional data without assuming orthogonality. In addition, SiBBIInGS enables BB interdependency or overlap, recognizes the existence of multiple trials within a state, and is capable of coping with trials of different duration or sampling rates. SiBBIInGS also offers both supervised and unsupervised versions to study the underlying state-similarity graphs, thus providing the user with the flexibility to choose between data-driven or predefined approaches based on their specific requirements and preferences. In particular, our framework employs a multi-view integra-

A Problem:

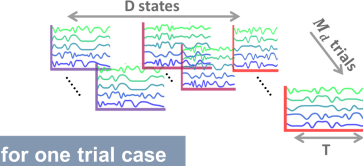
Y: observations across states, durations, sessions



A: Building Block matrices



Phi^T: temporal activity across sessions



B Goal: $Y \sim \hat{Y}$

$\forall d \in [1, D], \forall m \in [1, M_d]:$

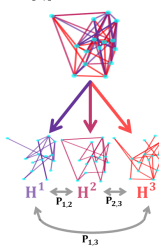
$$Y_m^d \approx \hat{Y}_m^d = A^d (\Phi_m^d)^T$$

$\in \mathbb{R}^{N \times T}$ $\in \mathbb{R}^{N \times p}$ $\in \mathbb{R}^{p \times T}$

C Calculate data-driven graphs

H: Channels Similarity

$$H_{[i,j]}^d = e^{-\|y_i^d - y_j^d\|_2^2}$$



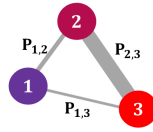
P: State Similarity

Supervised:

$$P_{d_1, d_2} = e^{-\|\Delta L\|_2^2}$$

Unsupervised:

$$P_{d_1, d_2} = e^{-\|\Delta y^{(d_1, d_2)}\|_2^2}$$



D Training demonstration for one trial case

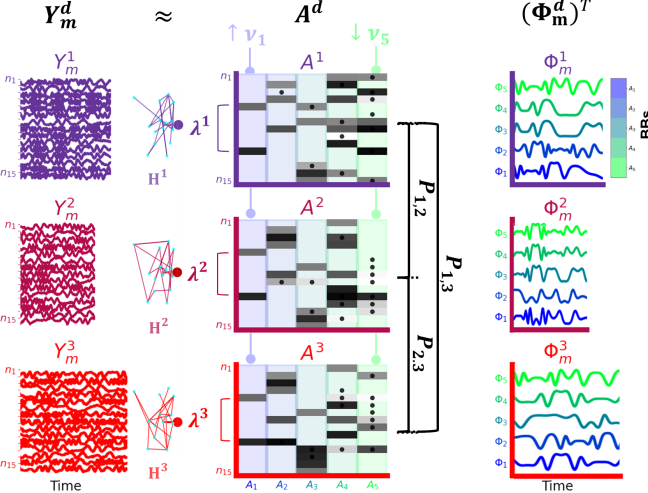


Figure 1: SiBBInGS model. **A:** Real-world datasets can contain variations in session duration or sampling rates and include data collected from the same system across multiple states with potentially different numbers of observations per state. SiBBInGS accommodates these degrees of variability by learning interpretable graph-driven per-state BBs and per-trials temporal activity for each BB. **B:** The SiBBInGS observation model is based on a per-state-and-trial matrix factorization where the BBs (A^d) are identical across trials and similar across states. **C:** BB similarity is controlled via data-driven channel graphs ($H^d \in \mathbb{R}^{N \times N}$) and a state-similarity graph ($P \in \mathbb{R}^{D \times D}$), which can be either predefined (supervised) or data-driven. **D:** Model learning schematic with three exemplary states and one exemplary trial per state. The BBs of each state d (columns of A^d) are constrained with two regularization terms. One (state-specific weighted λ^d) captures similar activity by leveraging a channel similarity graph H^d . The second, P , captures BB consistency across states via the state similarity graph. The vector ν controls the relative level of cross-state similarity between BBs, allowing for both background and state-specific BBs. Higher (lower) ν values promote greater (lesser) consistency of BBs across states (e.g. ν_1 v.s ν_5).

tion approach based on dictionary learning that incorporates a regularization term to group channels (e.g., neurons in neural recordings, genes in gene expression data) together based on their shared temporal activity.

Notations: Let $Y^d = \{Y_m^d\}_{m=1}^{M_d}$ denote a set of M_d trials for a given state d . The observation matrix $Y_m^d \in \mathbb{R}^{N \times T_m^d}$ for trial m and state d consists of N channels and T_m^d time points, such that the number of time points in each trial and across states can vary. A general dataset consists of a collection $\{Y_{m_1}^1\}_{m_1=1}^{M_1}, \dots, \{Y_{m_D}^D\}_{m_D=1}^{M_D}$ of D sets of trials, where each set of trials was collected under a different condition or state $d \in \{1, \dots, D\}$. This general dataset can represent, for instance, neural recordings of N neurons across D different tasks, or N is the measured gene expression levels across D different biological conditions. We model each individual trial as $Y_m^d = A^d (\Phi_m^d)^T + \epsilon_m^d$, with $A^d \in \mathbb{R}^{N \times p}$, $\Phi_m^d \in \mathbb{R}^{p \times T_m^d}$, where ϵ_m^d is an *i.i.d.* Gaussian sensor noise, and the model hyperparameter p sets the maximum number of desired BBs. Each A^d represents the BBs (as columns of the matrix) that are constant across trials of the same state but that can include small variations across states. The columns of Φ_m^d represent the corresponding temporal traces for a given state d and trial m .

Algorithm 1 SiBBInGS Model Training (short version)

Inputs

$\{\mathbf{Y}_m\}_{m=1:M_1}^1, \dots, \{\mathbf{Y}_m\}_{m=1:M_D}^D$ \triangleright Observations under D states, M_d trials for state d
 $\{\beta, \xi, \epsilon, \gamma_1, \gamma_2, \gamma_3, \gamma_4, \nu, K, w_{graph}, \sigma_p, \sigma_H\}, L$ (optional labels) \triangleright Model parameters

Initialization and pre-Calculations

$\mathbf{A}^d, \{\Phi_m^d\}_{m=1:M_d} \quad \forall d = 1 \dots D$ \triangleright Initialize BBs and temporal matrices
 $\mathbf{P} \in \mathbb{R}^{D \times D}, \mathbf{H} \in \mathbb{R}^{N \times N \times D}$ \triangleright Calculate similarity graphs via Eq. (3), (1), and (2).
while not all states converged **do** \triangleright Repeat until convergence of all states
 for all $d = 1 \dots D$ **do** \triangleright Iterate over states
 Select a random batch of trials from state d \triangleright Take a batch
 Update \mathbf{A}^d and λ^d \triangleright via Eq. (4)
 for all $m = 1 \dots M_d$ **do** \triangleright for every trial in the state
 update Φ_m^d \triangleright via Eq. (6)

Importantly, throughout the rest of the paper, we will adopt the following notations: superscript $()^d$ refers to state d , and subscript $()_m$ refers to trial m . Specifically, Y_m^d and Φ_m^d denote the observations and temporal traces of trial m of state d , while \mathbf{A}^d represents the BBs of state d (refer to Table 1 for detailed notation information). Additionally, for a general matrix \mathbf{Z} , let \mathbf{Z}_i , $(\mathbf{Z}_{:,j})$ denote the i -th row (j -th column) of a matrix \mathbf{Z} . With this data model, SiBBInGS aims to identify per-state \mathbf{A} and per-trial Φ , while ensuring similarity constraints among the \mathbf{A} s across states.

3.1 Model fitting

We develop a dictionary learning-like iterative procedure that alternates between updating the BBs $\{\mathbf{A}^d\}_d$ and their temporal profiles $\{\Phi_m^d\}_d$ for $d = 1 \dots D$. Critical to our approach is to identify non-Euclidean relationships between channels and between states. We thus augment the model with two graphs, one over channels, and one over states, to capture these relationships. The graph over channels is used in the update over $\{\mathbf{A}^d\}_d$ to identify regularities between channels,

and the states graph is used to promote consistency in BB structure across states. Mathematically, we formulate the fitting procedure as minimizing the following cost function to obtain $\{\hat{\mathbf{A}}^d\}_d, \{\hat{\Phi}_m^d\}_{m,d}$ for all $d = 1 \dots D$:

$$\min_{\{\mathbf{A}^d\}_d, \{\Phi_m^d\}_d} \sum_d^D \left(\sum_m^{M_d} [\|\mathbf{Y}_m^d - \mathbf{A}^d(\Phi_m^d)^T\|_F^2 + \mathcal{R}(\Phi_m^d)] + \mathcal{R}(\mathbf{A}^d) + \sum_{d' \neq d}^D P_{d,d'} \|(\mathbf{A}^d - \mathbf{A}^{d'})\mathbf{V}\|_2^2 \right)$$

where the first term is a data fidelity term, the second regularizes the BBs' temporal traces, the regularization $\mathcal{R}(\mathbf{A}^d)$ regularizes each BB to group channels based on shared temporal activity and to be sparse (as described in the next sections), and the last term regularizes BBs to be similar across states. The square matrix $\mathbf{P} \in \mathbb{R}^{D \times D}$ is a state-similarity graph that determines the effect of the similarity between each pair of states on the regularization of the distance between their BB representations, and can be set manually (supervised \mathbf{P}) or in a data-driven way (unsupervised \mathbf{P}), thus allowing selection based on specific goals, data type, and knowledge of data labels. Each of these two options offers unique benefits: the supervised variant enables explicit regulation of the similarity and the incorporation of important knowledge into the model based on human-expert familiarity with the data, whereas the unsupervised variant leverages the data itself to learn similarities and patterns, and is advantageous for learning data patterns without preconceived biases. The use of the matrix $\mathbf{V} = \text{diag}(\nu) \in \mathbb{R}^{p \times p}$, accompanied by the weight vector $\nu \in \mathbb{R}^p$, allows for assigning varying weights to individual BBs, thereby facilitating the creation of state-invariant vs state-specific BBs. The full model training is presented in Figure 1 and Algorithm 1.

3.2 Updating $\{\mathbf{A}^d\}$:

For the update of \mathbf{A} , we first define a state similarity graph, \mathbf{P} , that will be leveraged in the update of \mathbf{A} . **Supervised \mathbf{P} selection:** The supervised version of our model is particularly useful when there exists prior knowledge or expectations regarding quantitative state values that can be leveraged to

integrate desired information into the model. In this version, a numerical label \mathbf{L}_d is associated with each state d and can provide valuable information for constructing the state-similarity graph \mathbf{P} .

For instance, vector labels can represent the x-y positions of different angles in a reaching task; in analyzing purchasing profiles in different countries, the labels can represent financial measures of the states, like GDP.

This way, the similarity $P_{d,d'}$ between each pair of states (d, d') is calculated based on the distance between the labels $(\mathbf{L}_d, \mathbf{L}_{d'})$ associated with these states:

$$P_{d,d'} = \exp(-\|\mathbf{L}_d - \mathbf{L}_{d'}\|_2^2 / \sigma_P^2), \quad (1)$$

where σ_P^2 controls how the similarities in labels scale to similarities in BBs. The supervised approach easily extends to both data with identical or different session duration, and it can also handle cases where categorical states are involved without assuming varying levels of similarity (see Supplementary, section 9.1.1).

Data-driven \mathbf{P} selection: In cases where prior knowledge about state similarity is uncertain or not available for integration into the model, SiBBIInGS also provides an unsupervised version that employs a data-driven approach to calculate \mathbf{P} based on the distance between data points across states.

Here, to simplify the description, we focus on the setting of having a single trial for each state ($M_d = 1$), and all trials are equal length ($T_1^d = T \forall d = 1 \dots D$). In this case, the similarity graph \mathbf{P} is constructed as

$$P_{d,d'} = \exp(-\|\mathbf{Y}_1^d - \mathbf{Y}_1^{d'}\|_F^2 / \sigma_P^2), \quad (2)$$

where σ_P controls the bandwidth of the kernel (more options and information about \mathbf{P} reconstruction are found in the Supplementary, section 9).

After this pre-calculation, the update of \mathbf{A}^d for each state d , is achieved via a modified Re-Weighted ℓ_1 Graph Filtering (RWL1-GF) [10] with a channel-similarity graph. The channel graph promotes channels with similar temporal activity to be grouped into the same BBs. In particular, let \mathbf{Y}^{d*} be a matrix of size $N \times (\sum_{m=1}^{M_D} T_m^d)$ of horizontally concatenated observations of all trials of state d , we can first calculate the similarity between channels n_i and n_j under state d by:

$$\tilde{H}_{n_i, n_j}^d = \exp(-\|\mathbf{Y}_{n_i}^{d*} - \mathbf{Y}_{n_j}^{d*}\|^2 / \sigma_{\tilde{H}}^2), \quad (3)$$

where $\sigma_{\tilde{H}}$ is a model hyperparameter that controls the kernel bandwidth.

To ensure that \mathbf{H}^d , the channel similarity for each state d incorporates observations from all other states, and to create a more robust description, we utilize the previously computed state-graph (\mathbf{P}) to re-weight \mathbf{H} along the third (states) dimension. Thus, to mitigate the influence of outliers and encourage the clustering of similarly behaving channels into the same BB, we construct \mathbf{H}^d by taking the weighted sum $\sum_{d'=1}^D P_{d,d'} \tilde{\mathbf{H}}^{d'}$ and keeping only the k largest values in each row, while the remainder are set to zero. We then symmetrize this kernel and row-normalize it so that its rows sum to 1 (see Supplementary section 10).

The BBs matrix, \mathbf{A}_d , is shared among trials within a state d , but may vary across states, assuming consistent underlying groups within states, but potential variations in the main components' structure across states.

Then, given the channel graph (\mathbf{H}^d) of each state d , we update the n -th row of each estimate $\mathbf{a}_n^d = \hat{\mathbf{A}}_n^d$ via a re-weighted procedure that alternates between updating $\hat{\mathbf{a}}_n^d$ and $\lambda_{n,j}^d$, according to:

$$\begin{aligned} \hat{\mathbf{a}}_n^d &= \arg \min_{\mathbf{a}_n^d} \|\mathbf{y}_n - \mathbf{a}_n^d (\Phi^{d*})^T\|_2^2 + \sum_{j=1}^P \lambda_{n,j}^d |\mathbf{a}_n^d| + \sum_{d' \neq d} P_{dd'} \|(\mathbf{a}_n^d - \mathbf{a}_n^{d'}) \circ \boldsymbol{\nu}\|_2^2, \quad (4) \\ \lambda_{n,j}^d &= \epsilon / (\beta + |\hat{\mathbf{A}}_{n,j}^d| + w_{\text{graph}} |\mathbf{H}_{n,:}^d \hat{\mathbf{A}}_{:,j}^d|), \end{aligned}$$

where $\mathbf{y}_n = \mathbf{Y}_{n,:}^{d*}$ are horizontally concatenated observations of a random subset of trials from state d and Φ^{d*} are the relevant BBs' temporal traces. \circ is element-wise multiplication, and β , ϵ , and w_{graph} are model hyperparameters that can be tuned independently. In practice, we solve (5) for a random subset of trials from state d since this improves robustness to trial variability and computation speed.

The weighted evolving regularization terms $\lambda \in \mathbb{R}^{N \times p \times D}$ are determined based on the channel connectivity graph \mathbf{H} and the captured BBs (\mathbf{A}), such that each term $\lambda_{n,j}^d$ represents the weighted regularization term on the n -th channel of the j -th BB in state d .

The incorporation of \mathbf{H} within the denominator of λ yields a significant effect. For a given state d , a strong correlation between the similarity values of channel n ($\mathbf{H}_{n,:}^d$) and the j -th BB ($\hat{\mathbf{a}}_n^d$) results in a decrease in $\lambda_{n,j}^d$. Consequently, there is reduced regularization on the value of this channel within this BB, promoting the inclusion of this channel within the BB. Conversely, when the correlation is weak, $\lambda_{n,j}^d$ increases, leading to a higher degree of regularization and potentially reducing the likelihood of including this channel within the BB. The unique implementation of the extended RWL1-GF framework promotes the representation of inter-channel connectivity within the BB grouping while simultaneously mitigating background activity, thereby manifesting its effectiveness in SiBBIInGS. Finally, each column of \mathbf{A} for each state is scaled such that its maximum absolute value is 1.

3.3 Update over Φ_m^d

The update step over Φ_m^d uses the current estimate of \mathbf{A}^d to re-estimate the temporal profile matrix Φ_m^d independently over each state d and trial m . Note that we do not enforce similarity in Φ_m^d to allow for flexibility in capturing differences across states and trials. Thus, for each trial m and state d , $\phi = \Phi_m^d$ is updated by solving the following minimization problem, inspired by [10], with the addition of a diffusion component

$$\begin{aligned} \hat{\phi} = \arg \min_{\phi \geq 0} & \|\mathbf{Y}_m^d - \mathbf{A}^d \phi^T\|_F^2 + \gamma_1 \|\phi\|_F^2 + \gamma_2 \|\phi - \hat{\phi}^{\text{iter}-1}\|_F^2 + \gamma_3 \|\phi - \hat{\phi}^{t-1}\|_F^2 \\ & + \gamma_4 \|(\phi^T \phi - \text{diag}(\phi^T \phi)) \circ \mathbf{D}\|_{sav} \end{aligned} \quad (5)$$

where *sav* stands for sum-of-absolute-values and $\mathbf{D} \in \mathbb{R}^{p \times p}$ is a normalization matrix where the entry at index $[i, j]$ is $\frac{1}{\|\phi_{:,i}\|_2 \|\phi_{:,j}\|_2}$. The first term above corresponds to the data fidelity term, which measures the similarity between the reconstructed dictionary and the original data, the second term is a regularization term that penalizes excessive activity, the third term encourages continuity in the dictionary across iterations by penalizing the difference between the current and previous iterations of the dictionary (where $\hat{\phi}^{\text{iter}-1}$ refers to ϕ from the previous model iteration), the fourth term is a diffusion term that promotes temporal consistency of the dictionary across consecutive samples (where $\hat{\phi}^{t-1}$ refers to a shifted version of ϕ by 1 time point), and the fifth and final term promotes decorrelation among the temporal traces by penalizing the sum of absolute values of the off-diagonal correlation matrix elements. The update step thus seeks to improve the dictionary by minimizing the cost function, while balancing sparsity, decorrelated elements, continuity, and temporal consistency (see Supplementary section 11 for how to solve the above in practice).

4 Experiments

4.1 SiBBIInGS recovers ground truth BBs in synthetic data

We first explore how well SiBBIInGS can recover ground truth BBs and time traces in simulated data. Synthetic data were generated with $D = 3$ states, each consisting of a single trial, $p = 10$ ground-truth BBs, and $N = 100$ channels. Each i -th BB was generated with a maximum cardinality of $\max_{d,i} |\mathbf{A}_{:,i}^d|_0 = 21$ channels, and on average, each channel was associated with 2.1 BBs. While the BBs were designed to be non-orthogonal, we constrained their pairwise correlations to be below a threshold of $\max \rho < 0.6$. The temporal dynamics of the synthetic data were generated by summing 15 trigonometric functions with different frequencies (see Supplementary section 13.2 for more details). SiBBIInGS exhibited a monotonically decreasing MSE during training (Fig. 5), and at convergence was able to successfully recover the underlying BBs in the synthetic data and their temporal traces (Fig 2A, B, C). Example traces demonstrate a high precision of the recovered temporal traces, with correlation to the ground truth traces being close to one (Fig. 2A, C). Furthermore, the identified BB components align closely with the ground truth BBs (Fig. 2B,C), as indicated by high Jaccard index values. Notably, tensor decomposition models, like PARAFAC, were unable to identify the BBs (Fig. 2E).

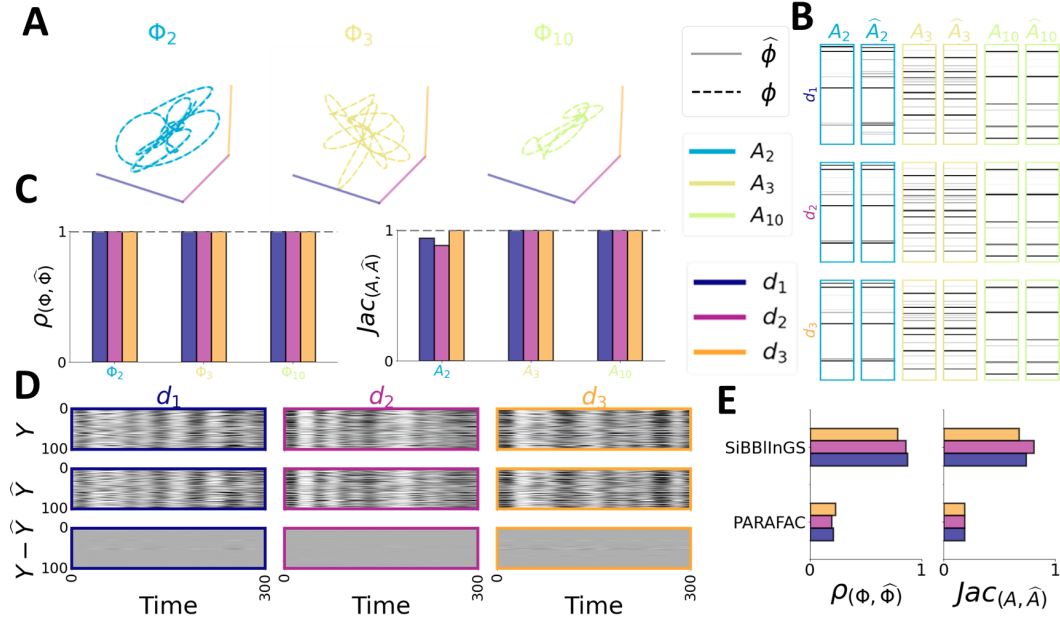


Figure 2: **Demonstration of SiBBIInGS on Synthetic Data.** **A** Three exemplary temporal traces as identified by SiBBIInGS vs the ground truth traces, projected onto the axes of the three synthetic states. This view facilitates the observation of traces highly correlated with specific states (e.g., Φ_{10} in green), as well as the identification of traces that exhibit similar activations across different states (e.g., Φ_2 in blue). **B** Comparison between the identified BBs and the ground truth BBs. **C** Correlation between the identified temporal traces and the ground truth traces (left), and Jaccard index of the identified BBs compared to the ground truth BBs (right). **D** Comparison between the ground truth data (top), the reconstruction by SiBBIInGS (middle), and the difference between them (bottom). **E** Comparison to PARAFAC (see Supplementary section 13.4).

4.2 SiBBIInGS finds interpretable BBs and temporal traces in Google Trends data

Google Trends [22] is a public web facility that allows users to query how often specific terms have been searched in Google over time. We leverage this rich dataset to showcase SiBBIInGS’ capability to identify meaningful temporal and structural patterns. We used a monthly Trends volume of 44 queries related to various topics as searched in 8 US states that were selected based on their diverse characteristics, population size, and culture [16]. The data cover the time period from Jan. 2011 to Oct. 2022, resulting in 142 months. The $p = 5$ BBs identified by SiBBIInGS reveal clusters of terms underlying differences in user interests, and the temporal traces convey how these interests evolve over time for each region (Fig. 3). The temporal traces (Fig. 3A) exhibit distinct patterns, which align with the expected seasonality of the BBs’ word components (Fig. 3B). For instance, the first BB represents college-related terms and shows a gradual decrease over the years, with periodic activity and a notable deviation during the COVID pandemic, possibly reflecting factors such as the shift to remote learning (see more details in Fig. 7 and section 14.3). The second and fourth BBs demonstrate distinct periodic patterns associated with their respective domains, such as Passover in April and Winter in December, accompanied by a consistent background activity. Interestingly, in CA, FL, and NY—all states with larger Jewish populations—the temporal peaks corresponding to the “Passover” (Jewish holiday celebrated around April) BB exhibit more pronounced peaks compared to the other states (Fig. 8).

The last identified BB represents COVID-related terms and exhibits a distinct temporal pattern with a sharp increase around January 2020, coinciding with the onset of the COVID pandemic in the US. Interestingly, the term “Hopkins” has a relatively smaller representation in MD (the blue circle), where the hospital is located. This may be attributed to the fact that the relevant hospital is already well-known there, leading to less variation in Google searches over time compared to other states. In states where Hopkins had less prominence prior to the pandemic, there was a significant surge in Hopkins-related searches at the beginning of the COVID outbreak, and hence present a larger

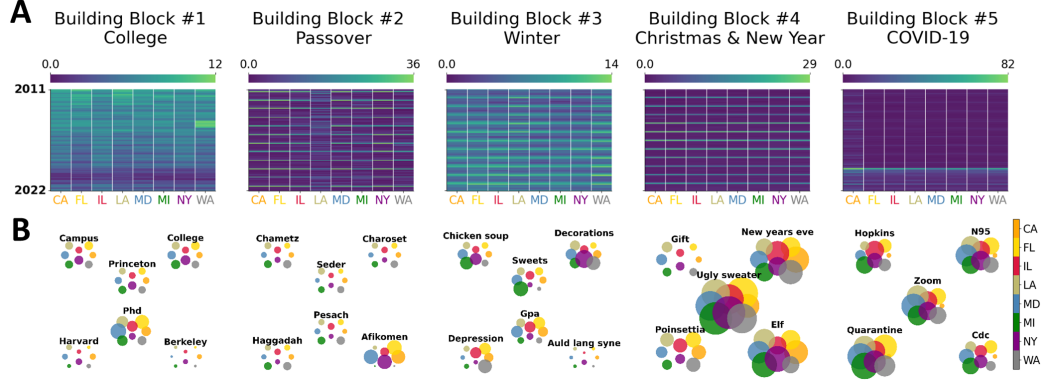


Figure 3: **Demonstration on Google Trends data.** **A** Temporal traces of the identified BBs demonstrate seasonal trends consistent with the words associated with each BB. **B** BBs by different states along with their dominance in each state. Different states are marked in different colors (see color-bar). Each dot size represents the contribution of the term in the associated BB.

dominance of this term in the COVID BB. This demonstration highlights the model’s interpretability in the context of online search, as the queries (channels) have discernible meaning. Moreover, these examples underscore the importance of capturing the natural variability in the data by identifying similar but potentially not identical BBs across states.

4.3 SiBBInGS identifies meaningful patterns in macaques’ neural recordings

Finally, we test SiBBInGS on neural activity recorded from Brodmann’s area 2 of the somatosensory cortex in a monkey performing a reaching task, as described by Chowdhury and Miller (2022) [14, 15]. The used data consist of 8 different hand angle directions, representing distinct states, with each angle comprising 18 trials observed under noisy conditions. The spike data were convolved using a Gaussian kernel over time, resulting in 57 time points for a trial. When applying SiBBInGS with a maximum of $p = 4$ BBs, we were able to identify sparse underlying BBs (Fig. 4B) captured based on the shared temporal activity of their participating neurons, along with meaningful temporal traces (Fig. 4D) that exhibit different patterns across states. Interestingly, the third BB consistently shows minimal activity across all states, suggesting it captures background or noise activity. Notably, the structure of the identified BBs, as revealed by SiBBInGS, exhibits subtle yet significant adaptations across states in terms of neuron weights and BB assignments. Furthermore, SiBBInGS supports the presence of neurons belonging to multiple neural clusters, suggesting their involvement in multiple functionalities.

When examining the temporal correlations of the same BB within and between states, all BBs exhibited a within/between ratio significantly greater than 1 (Fig. 4E, Supplementary Fig. 10, and section 15.4). This indicates reduced variability within states and clear distinctions between states. Furthermore, when using the temporal traces as the sole input for a simple multi-class logistic regression model, accurate state predictions were achieved with high accuracy, as illustrated in the confusion matrix in Figure 4C.

5 Conclusions and discussion

In this paper, we propose SiBBInGS, a framework for identifying interpretable building blocks (BBs) and their temporal profiles in high-dimensional time-series data collected across multiple states and trials. SiBBInGS leverages channel-similarity and state-similarity graphs to identify interpretable BBs obscured in the data and thus provides insights into the structure and variability of the system activity. By harnessing SiBBInGS, we can gain valuable insights into functional circuits, task encoding, and state modulations across various data modalities, making it applicable to diverse fields such as neuroscience, social science, genetics, and beyond. One of the key advantages of SiBBInGS is its ability to naturally and flexibly deal with variability in 1) the number of trials within states, 2) trial duration, 3) the activation of BBs across states, and 4) subtle changes in the BBs them-

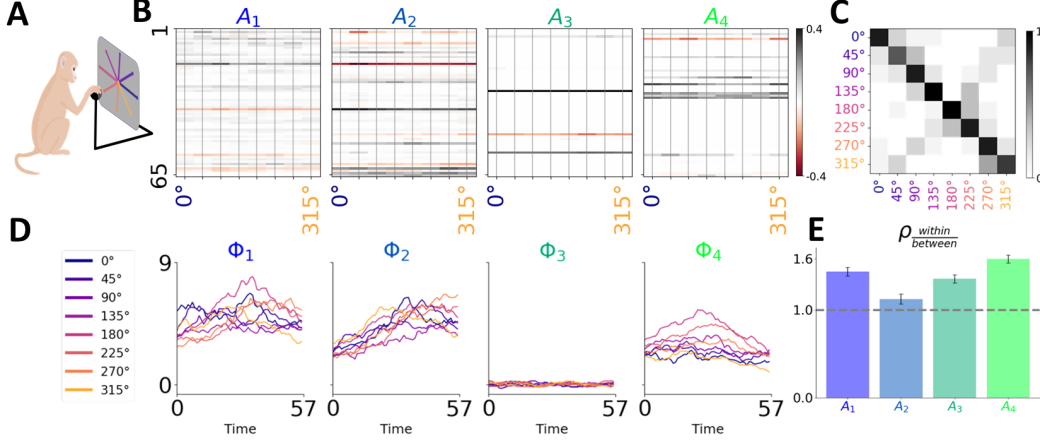


Figure 4: **Identification of Temporal Patterns in Monkey Somatosensory Cortex.** **A** Illustration of the reaching out task (monkey image from [48]). **B** Sparse clusters of neurons representing identified BBs. **C** Confusion matrix of a logistic regression model using the inferred temporal traces to predict the state label. **D** The identified BB’s temporal traces as they vary across states (different colors) and time. **E** Ratios of the within-state temporal correlation to between-state correlations for each BB. $\rho_{within}/\rho_{between} > 1$, indicating distinguishability between states.

selves between states. By accommodating such variability, SiBBIInGS is well-suited for analyzing complex, real-world datasets collected in diverse experimental settings. Unlike many existing methods that assume orthogonality, SiBBIInGS can find interpretable sparse representations of the data based on temporal relationships between the BBs. Moreover, SiBBIInGS goes beyond current DL techniques by incorporating what are, in essence, multi-way graphs to capture relationships across channels and states simultaneously.

Limitations: We note a number of limitations with our current model that warrant additional future work. For one, our current approach is limited to the least-squares setting, while a Poisson, or calcium imaging likelihood would potentially improve applications to broader neural datasets. Furthermore, we have restricted this work to a specific graph construction, potentially limiting the ability to account for higher-order BB inter-dependencies (e.g., akin to group-sparse coding). One specific avenue in this direction is to explore more advanced distance metrics for graph learning in the case of varying trial duration, e.g., via more advanced time-warping techniques [61]. Furthermore, we explored here both a supervised and unsupervised method of inter-state similarity graphs. At times, similarity labels are available but with low certainty, recommending a current limitation and future extension towards a hybrid approach that combines the labels and data-driven graphs.

6 Data and code availability

The data used in this study are publicly available, and the code can be found on GitHub at <https://github.com/NogaMudrik/SiBBIInGS>.

7 Acknowledgments

N.M. was supported by the Kavli Foundation Kavli Discovery Award. G.M. was partially supported by NIH grant R01EB026936.

References

- [1] Michal Aharon, Michael Elad, and Alfred Bruckstein. K-svd: An algorithm for designing overcomplete dictionaries for sparse representation. *IEEE Transactions on Signal Processing*, 54(11):4311–4322, 2006.
- [2] Hadeel K Aljobouri. Independent component analysis with functional neuroscience data analysis. *Journal of Biomedical Physics and Engineering*, 2023.
- [3] Mikio Aoi and Jonathan W Pillow. Model-based targeted dimensionality reduction for neuronal population data. *Advances in Neural Information Processing Systems*, 31, 2018.
- [4] Mikio C Aoi, Valerio Mante, and Jonathan W Pillow. Prefrontal cortex exhibits multidimensional dynamic encoding during decision-making. *Nature Neuroscience*, 23(11):1410–1420, 2020.
- [5] Ziv Bar-Joseph, Anthony Gitter, and Itamar Simon. Studying and modelling dynamic biological processes using time-series gene expression data. *Nature Reviews Genetics*, 13(8):552–564, 2012.
- [6] Donald J Berndt and James Clifford. Using dynamic time warping to find patterns in time series. In *Proceedings of the 3rd International Conference on Knowledge Discovery and Data Mining*, pages 359–370. AAAI Press, 1994.
- [7] Julius H Bourke and Matthew B Wall. phmri: methodological considerations for mitigating potential confounding factors. *Frontiers in Neuroscience*, 9:167, 2015.
- [8] Emmanuel J Candes, Michael B Wakin, and Stephen P Boyd. Enhancing sparsity by reweighted ℓ_1 minimization. *Journal of Fourier analysis and applications*, 14:877–905, 2008.
- [9] Adam S Charles, Aurele Balavoine, and Christopher J Rozell. Dynamic filtering of time-varying sparse signals via ℓ_1 minimization. *IEEE Transactions on Signal Processing*, 64(21):5644–5656, 2016.
- [10] Adam S Charles, Nathan Cermak, Rifqi O Affan, Benjamin B Scott, Jackie Schiller, and Gal Mishne. Graft: Graph filtered temporal dictionary learning for functional neural imaging. *IEEE Transactions on Image Processing*, 31:3509–3524, 2022.
- [11] Adam S Charles, Mijung Park, J Patrick Weller, Gregory D Horwitz, and Jonathan W Pillow. Dethroning the fano factor: a flexible, model-based approach to partitioning neural variability. *Neural Computation*, 30(4):1012–1045, 2018.
- [12] Adam S Charles and Christopher J Rozell. Spectral superresolution of hyperspectral imagery using reweighted ℓ_1 spatial filtering. *IEEE Geoscience and Remote Sensing Letters*, 11(3):602–606, 2013.
- [13] Po-Hsuan (Cameron) Chen, Janice Chen, Yaara Yeshurun, Uri Hasson, James Haxby, and Peter J Ramadge. A reduced-dimension fmri shared response model. In C. Cortes, N. Lawrence, D. Lee, M. Sugiyama, and R. Garnett, editors, *Advances in Neural Information Processing Systems*, volume 28. Curran Associates, Inc., 2015.
- [14] Raed Chowdhury and Lee Miller. Area2.bump: macaque somatosensory area 2 spiking activity during reaching with perturbations. Data set, 2022.
- [15] Raed H Chowdhury, Joshua I Glaser, and Lee E Miller. Area 2 of primary somatosensory cortex encodes kinematics of the whole arm. *Elife*, 9:e48198, 2020.
- [16] David Coulby. *Beyond the national curriculum: Curricular centralism and cultural diversity in Europe and the USA*. Psychology Press, 2000.
- [17] Lieven De Lathauwer, Bart De Moor, and Joos Vandewalle. Multilinear subspace learning: dimensionality reduction of multidimensional data. In *Proceedings of the 2000 Conference on Advances in Neural Information Processing Systems*, pages 485–491, 2000.

- [18] Lea Duncker and Maneesh Sahani. Temporal alignment and latent gaussian process factor inference in population spike trains. *Advances in Neural Information Processing Systems*, 31, 2018.
- [19] Pierre Garrigues and Bruno Olshausen. Group sparse coding with a Laplacian scale mixture prior. *Advances in Neural Information Processing Systems*, 23, 2010.
- [20] Nabeel Gillani and Rebecca Eynon. Understanding and improving social factors in education: a computational social science approach. *arXiv preprint arXiv:2301.05619*, 2023.
- [21] Gene H Golub and Charles F Van Loan. *Matrix computations*. JHU press, 2013.
- [22] Google Trends. Google Trends. <https://trends.google.com/trends/>, Accessed 11 November 2022.
- [23] Krzysztof J Gorgolewski, Amos J Storkey, Mark E Bastin, Ian Whittle, and Cyril Pernet. Single subject fmri test–retest reliability metrics and confounding factors. *Neuroimage*, 69:231–243, 2013.
- [24] Robbe LT Goris, J Anthony Movshon, and Eero P Simoncelli. Partitioning neuronal variability. *Nature Neuroscience*, 17(6):858–865, 2014.
- [25] JC Gower. Dijksterhuis, gb: Procrustes problems, 2004.
- [26] Richard A Harshman. Foundations of the parafac procedure: Models and conditions for an “explanatory” multimodal factor analysis. *UCLA Working Papers in Phonetics*, 16(1):1–84, 1970.
- [27] Hong He, Yonghong Tan, and Wuxiong Zhang. A wavelet tensor fuzzy clustering scheme for multi-sensor human activity recognition. *Engineering Applications of Artificial Intelligence*, 70:109–122, 2018.
- [28] Harold Hotelling. Analysis of a complex of statistical variables into principal components. *Journal of educational psychology*, 24(6):417, 1933.
- [29] Aapo Hyvarinen, J Karhunen, and E Oja. Independent component analysis and blind source separation, 2001.
- [30] Connor T Jerzak, Gary King, and Anton Strezhnev. An improved method of automated non-parametric content analysis for social science. *Political Analysis*, 31(1):42–58, 2023.
- [31] Rahul Kala, Anupam Shulkla, and Ritu Tiwari. Fuzzy neuro systems for machine learning for large data sets. In *2009 IEEE International Advance Computing Conference*, pages 541–545. IEEE, 2009.
- [32] EG Kogbetliantz. Solution of linear equations by diagonalization of coefficients matrix. *Quarterly of Applied Mathematics*, 13(2):123–132, 1955.
- [33] Jean Kossaifi, Yannis Panagakis, Anima Anandkumar, Maja Atanasijevic, Nikolaos Balntas, Andrei Bursuc, Siyu Chen, Theodore Cohen, Emile Contal, Benoit Couellan, Khalid El Housni, Dariusz Krol, Evgenia Kusmenko, David Marteau, Alexandru Mocanu, Mickael Perrot, Antoine Prouvost, Roman Remme, Justus Schock, and Kiran R. Varikooty. TensorLy: Tensor learning in python. <http://tensorly.org/stable/>, 2021.
- [34] Daniel D Lee and H Sebastian Seung. Learning the parts of objects by non-negative matrix factorization. *Nature*, 401(6755):788–791, 1999.
- [35] Ran Liu, Mehdi Azabou, Max Dabagia, Jingyun Xiao, and Eva Dyer. Seeing the forest and the tree: Building representations of both individual and collective dynamics with transformers. *Advances in Neural Information Processing Systems*, 35:2377–2391, 2022.
- [36] Valerio Mante, David Sussillo, Krishna V Shenoy, and William T Newsome. Context-dependent computation by recurrent dynamics in prefrontal cortex. *Nature*, 503(7474):78–84, 2013.

- [37] Gal Mishne and Adam S Charles. Learning spatially-correlated temporal dictionaries for calcium imaging. In *ICASSP 2019-2019 IEEE International Conference on Acoustics, Speech and Signal Processing (ICASSP)*, pages 1065–1069. IEEE, 2019.
- [38] Gal Mishne, Ronen Talmon, Ron Meir, Jackie Schiller, Maria Lavzin, Uri Dubin, and Ronald R. Coifman. Hierarchical coupled-geometry analysis for neuronal structure and activity pattern discovery. *IEEE Journal of Selected Topics in Signal Processing*, 10(7):1238–1253, 2016.
- [39] Noga Mudrik, Yenho Chen, Eva Yezerets, Christopher J Rozell, and Adam S Charles. Decomposed linear dynamical systems (dlds) for learning the latent components of neural dynamics. *arXiv preprint arXiv:2206.02972*, 2022.
- [40] Ramon Nogueira, Sofia Lawrie, and Rubén Moreno-Bote. Neuronal variability as a proxy for network state. *Trends in Neurosciences*, 41(4):170–173, 2018.
- [41] Bruno A Olshausen and David J Field. Wavelet-like receptive fields emerge from a network that learns sparse codes for natural images. *Nature*, 381:607–609, 1996.
- [42] Bruno A Olshausen and David J Field. Sparse coding of sensory inputs. *Current Opinion in Neurobiology*, 14(4):481–487, 2004.
- [43] The pandas development team. pandas-dev/pandas: Pandas, February 2020.
- [44] Fabian Pedregosa, Gaël Varoquaux, Alexandre Gramfort, Vincent Michel, Bertrand Thirion, Olivier Grisel, Mathieu Blondel, Peter Prettenhofer, Ron Weiss, Vincent Dubourg, Jake Vanderplas, Alexandre Passos, David Cournapeau, Matthieu Brucher, Matthieu Perrot, and Édouard Duchesnay. Scikit-learn: Machine learning in Python. *Journal of Machine Learning Research*, 12:2825–2830, 2011.
- [45] Felix Pei, Joel Ye, David M. Zoltowski, Anqi Wu, Raed H. Chowdhury, Hansem Sohn, Joseph E. O’Doherty, Krishna V. Shenoy, Matthew T. Kaufman, Mark Churchland, Mehrdad Jazayeri, Lee E. Miller, Jonathan Pillow, Il Memming Park, Eva L. Dyer, and Chethan Pandarinath. Neural latents benchmark ’21: Evaluating latent variable models of neural population activity. In *Advances in Neural Information Processing Systems (NeurIPS), Track on Datasets and Benchmarks*, 2021.
- [46] Jing Qin, Shuang Li, Deanna Needell, Anna Ma, Rachel Grotheer, Chenxi Huang, and Natalie Durgin. Stochastic greedy algorithms for multiple measurement vectors. *arXiv preprint arXiv:1711.01521*, 2017.
- [47] M. Ravasi and I. Vasconcelos. Pylops—a linear-operator python library for scalable algebra and optimization. *SoftwareX*, 11:100495, 2020.
- [48] Andrea Colins Rodriguez. Monkey (arm movement), 2023.
- [49] Chris Rorden and Hans-Otto Karnath. Using human brain lesions to infer function: a relic from a past era in the fmri age? *Nature Reviews Neuroscience*, 5(10):812–819, 2004.
- [50] Peter J Schmid. Dynamic mode decomposition of numerical and experimental data. *Journal of Fluid Mechanics*, 656:5–28, 2010.
- [51] Steffen Schneider, Jin Hwa Lee, and Mackenzie Weygandt Mathis. Learnable latent embeddings for joint behavioural and neural analysis. *Nature*, pages 1–9, 2023.
- [52] Khandakar Tanvir Ahmed, Sze Cheng, Qian Li, Jeongsik Yong, and Wei Zhang. Incomplete time-series gene expression in integrative study for islet autoimmunity prediction. *Briefings in Bioinformatics*, 24(1):bbac537, 2023.
- [53] Ivana Tošić and Pascal Frossard. Dictionary learning. *IEEE Signal Processing Magazine*, 28(2):27–38, 2011.
- [54] Hossein Valavi and Peter J Ramadge. Multi-dataset low-rank matrix factorization. In *2019 53rd Annual Conference on Information Sciences and Systems (CISS)*, pages 1–5. IEEE, 2019.

- [55] Ewout van den Berg and Michael P. Friedlander. Probing the pareto frontier for basis pursuit solutions. *SIAM Journal on Scientific Computing*, 31(2):890–912, 2008.
- [56] Pauli Virtanen, Ralf Gommers, Travis E. Oliphant, Matt Haberland, Tyler Reddy, David Cournapeau, Evgeni Burovski, Pearu Peterson, Warren Weckesser, Jonathan Bright, Stéfan J. van der Walt, Matthew Brett, Joshua Wilson, K. Jarrod Millman, Nikolay Mayorov, Andrew R. J. Nelson, Eric Jones, Robert Kern, Eric Larson, C J Carey, İlhan Polat, Yu Feng, Eric W. Moore, Jake VanderPlas, Denis Laxalde, Josef Perktold, Robert Cimrman, Ian Henriksen, E. A. Quintero, Charles R. Harris, Anne M. Archibald, Antônio H. Ribeiro, Fabian Pedregosa, Paul van Mulbregt, Ashwin Vijaykumar, Alberto Bardelli, Adrian Rothberg, Andreas Hilboll, Andreas Kloeckner, and SciPy 1.0 Contributors. SciPy 1.0: fundamental algorithms for scientific computing in Python. *Nature Methods*, 17:261–272, 2020.
- [57] Huiqin Wei, Long Chen, Keyu Ruan, Lingxi Li, and Long Chen. Low-rank tensor regularized fuzzy clustering for multiview data. *IEEE Transactions on Fuzzy Systems*, 28(12):3087–3099, 2020.
- [58] Wes McKinney. Data Structures for Statistical Computing in Python. In Stéfan van der Walt and Jarrod Millman, editors, *Proceedings of the 9th Python in Science Conference*, pages 56 – 61, 2010.
- [59] Benjamin White, Larry F Abbott, and József Fiser. Suppression of cortical neural variability is stimulus-and state-dependent. *Journal of Neurophysiology*, 108(9):2383–2392, 2012.
- [60] Alex H Williams, Tony Hyun Kim, Forea Wang, Saurabh Vyas, Stephen I Ryu, Krishna V Shenoy, Mark Schnitzer, Tamara G Kolda, and Surya Ganguli. Unsupervised discovery of demixed, Low-Dimensional neural dynamics across multiple timescales through tensor component analysis. *Neuron*, 98(6):1099–1115.e8, June 2018.
- [61] Alex H Williams, Ben Poole, Niru Maheswaranathan, Ashesh K Dhawale, Tucker Fisher, Christopher D Wilson, David H Brann, Eric M Trautmann, Stephen Ryu, Roman Shusterman, et al. Discovering precise temporal patterns in large-scale neural recordings through robust and interpretable time warping. *Neuron*, 105(2):246–259, 2020.
- [62] M-S Yang. A survey of fuzzy clustering. *Mathematical and Computer Modelling*, 18(11):1–16, 1993.
- [63] Robert J Zatorre, R Douglas Fields, and Heidi Johansen-Berg. Plasticity in gray and white: neuroimaging changes in brain structure during learning. *Nature Neuroscience*, 15(4):528–536, 2012.
- [64] Zhilin Zhang and Bhaskar D Rao. Sparse signal recovery with temporally correlated source vectors using sparse bayesian learning. *IEEE Journal of Selected Topics in Signal Processing*, 5(5):912–926, 2011.

Supplementary Material

8 Notations

Table 1: List of notations for SiBBLINGS.

Symbol	Description
BBs	Building Blocks
channels	Each feature in the observations, e.g., neurons in recordings
states	Different "views" of the observations. e.g. different cognitive tasks
trials/sessions	Repeated observations within state
p	Number of BBs
D	Number of states
M_d	Number of trials for state d
N	Number of channels
\mathbf{Z}_n : (or $\mathbf{Z}_{[n,:]}$)	The n -th row of a general matrix \mathbf{Z}
$\mathbf{Z}_{:i}$ (or $\mathbf{Z}_{[:,i]}$)	The i -th column of a general matrix \mathbf{Z}
L_d	Label of state d (optional, can be a scalar or a vector)
$\mathbf{Y}_m^d \in \mathbb{R}^{N \times T_m^d}$	Observation for trial m and state d
$\mathbf{A}^d \in \mathbb{R}^{N \times p}$	Matrix of BBs for state d .
$\Phi_m^d \in \mathbb{R}^{N \times T_m^d}$	Matrix of temporal traces for trial m of state d .
$\mathbf{P} \in \mathbb{R}^{D \times D}$	States similarity graph
$\mathbf{H} \in \mathbb{R}^{N \times N \times D}$	Channel similarity graph
$\boldsymbol{\nu} \in \mathbb{R}^p$	Controls the relative level of cross-state similarity for each BB
$\mathbf{V} = \text{diag}(\boldsymbol{\nu})$	A diagonal matrix whose entry in index ii is the i -th entry of $\boldsymbol{\nu}$
β	An hyperparameter controlling the strength of regularization
$\gamma_1, \gamma_2, \gamma_3, \gamma_4$	Hyperparameters to regularize Φ_m^d
$\sigma_{\widetilde{\mathbf{H}}}, \sigma_{\mathbf{P}}$	Hyperparameters that control the bandwidth of the kernel
$\psi_n^{ij} \in \mathbb{R}^{M_j, M_i}$	Transformation of the data from state i to state j for channel n

9 Further options for P computation

Here, we explore additional approaches for computing the state-similarity graph P . These options take into account factors like data properties, single vs. multi-trial cases, variations in trial duration, and the desired approach (supervised or data-driven).

9.1 Supervised P

9.1.1 Categorical or Similar-Distanced States

For cases where observation states are represented by categorical labels, and we expect a high degree of similarity between all possible pairs of states (i.e., no pair of labels is closer to each other than to another pair), we can define the state similarity matrix P to be identical for all pairs of states. P is then constructed as

$$\mathbf{P} = \mathbf{1} \otimes \mathbf{1}^T + c\mathbf{I}, \quad (5)$$

where $\mathbf{P} = \mathbf{1} \otimes \mathbf{1}^T \in \mathbb{R}^{D \times D}$ is a matrix of all ones, $\mathbf{I} \in \mathbb{R}^{D \times D}$ is the identity matrix, and c is a weight that scales the strength of self-similarity with respect to cross-state similarities.

9.2 Data Driven P

Here we discuss three different options for constructing the matrix P in a data-driven manner, depending on the structure of the observations.

9.2.1 Multiple trials per state, same trial duration

In the most general case where all trials have the same temporal duration, the similarity matrix P is computed by evaluating the distance between the values of each pair of states, considering all trials

within each state. For this, we first find the transformation $\psi_n^{ij} \in \mathbb{R}^{M_j \times M_i}$ between the observations of state i to the observation of state j , by solving the Orthogonal Procrustes problem [21, 25]. For this, let $\mathbf{Y}^{i*} \in \mathbb{R}^{M_i \times (T \times N)}$ be the matrix obtained by vertically concatenating the flattened observations from each trial ($m = 1 \dots M_i$) of state i . Then, the optimal transformation from the observations of state i ($\mathbf{Y}^{i*} \in \mathbb{R}^{M_i \times (T \times N)}$) to the observations of state j ($\mathbf{Y}^{j*} \in \mathbb{R}^{M_j \times (T \times N)}$) will be

$$\hat{\psi}^{ij} = \arg \min_{\psi^{ij}} \|\psi^{ij} \mathbf{Y}^{i*} - \mathbf{Y}^{j*}\|_F^2,$$

where this mapping projects the multiple trials of state i into the same space as of state j , via $\tilde{\mathbf{Y}}^{i*} = \hat{\psi}^{ij} \mathbf{Y}^{i*}$. The state similarity matrix will thus be

$$\mathbf{P}_{ij} = \exp \left(-\|\tilde{\mathbf{Y}}^{i*} - \mathbf{Y}^{j*}\|_F^2 / \sigma_p^2 \right), \quad (5)$$

for all states $i, j = 1 \dots D$, and where σ_p controls the kernel bandwidth.

9.2.2 Single-trial per state, different duration

Further generalization of the state similarity computation requires addressing the case of trials being of varying duration. When the observations correspond to the same process and their alignment using dynamic time warping is justifiable, we can replace the Gaussian kernel measure with the Dynamic Time Warping (DTW) distance metric [6]. When we observe a single trial for each state, the similarity metric becomes the average DTW distances over all channels,

$$\mathbf{P}_{ij} = \exp \left(-\frac{1}{N} \sum_{n=1}^N DTW(\mathbf{Y}_{n:}^i, \mathbf{Y}_{n:}^j) \right). \quad (5)$$

9.2.3 Multiple trials per state, different duration

Similarly, for the multi-trial case we have

$$\mathbf{P}_{ij} = \exp \left(-\frac{1}{N} \sum_{n=1}^N \left(\frac{1}{M_j} \sum_{m=1}^{M_j} DTW \left((\tilde{\mathbf{Y}}^{i*})_{m, [(n-1)T:nT]}, (\mathbf{Y}^{j*})_{m, [(n-1)T:nT]} \right) \right) \right), \quad (5)$$

where, as before, \mathbf{Y}^{j*} is the stacked-trials version of the observations at state j in channel n , such that $(\mathbf{Y}^{j*})_{m:}$ is the m -th row of this matrix, and $(\mathbf{Y}^{j*})_{m, [(n-1)T:nT]}$ corresponds to the m -th row of this matrix, but limited to the columns ranging from $(n-1)T$ to nT . $\tilde{\mathbf{Y}}^{i*}$, as before, refers to the re-ordered version of \mathbf{Y}^{i*} according to \mathbf{Y}^{j*} . It is crucial to note that this approach operates under the assumption that the trials being compared depict similar processes, and that aligning them using DTW is a valid assumption. By aligning the rows using DTW, we can assess the dissimilarity between the trials while accommodating potential temporal distortions and variations in the time axis.

10 Channel-similarity kernel (\mathbf{H})—generation and processing

The kernel post-processing involves several steps. First, we construct the kernel $\tilde{\mathbf{H}}^d$ for each state $d = 1 \dots D$, as described in Equation (1). To incorporate similarities between each possible pair of states $d' \neq d$, where $d, d' = 1 \dots D$, we perform a weighted average of each \mathbf{H}^d with the kernels of all other states, using \mathbf{P}_d for the weights, as it quantifies the similarity between state d and all other states: $\mathbf{H}^d = \sum_{d'}^D \mathbf{P}_{dd'} \tilde{\mathbf{H}}^{d'}$. Then, to promote a more robust algorithm, we only retain the k highest values (i.e., k-Nearest Neighbors; kNN) in each row, while the rest are set to zero. The value of k is a model hyperparameter, and depends on the desired BB size. We then symmetrize each state's kernel by calculating $\mathbf{H}^d \leftarrow \frac{1}{2} (\mathbf{H}^d + (\mathbf{H}^d)^T)$ for all $d = 1 \dots D$. Finally, the kernel is row-normalized so that each row sums to one, as follows: Let Λ^d be a diagonal matrix with elements representing the row sums of \mathbf{H}^d , i.e., $\Lambda_{ii}^d = \text{diag} \left(\sum_{n=1}^N \mathbf{H}_{i,n}^d \right)$. The final normalized channel similarity kernel is obtained as $\mathbf{H}_{\text{final}}^d = (\Lambda^d)^{-1} \mathbf{H}^d$.

11 Solving Φ in practice

In Section 3.3, the model updates the temporal traces dictionary $\phi = \Phi_m^d$ for all $m = 1 \dots M_d$, $d = 1 \dots D$ using an extended least squares for each time point t , i.e.,

$$\tilde{\phi}_{[t,:]} = \arg \min_{\phi_{[t,:]}} \|\tilde{\mathbf{Y}}_{m[t,:]}^d - \tilde{\mathbf{M}}\phi_{[t,:]} \|_2^2, \quad (5)$$

where $\phi_{[t,:]} \in \mathbb{R}^p$ is the dictionary at time t ,

$$\tilde{\mathbf{Y}}_{m[t,:]}^d = \begin{bmatrix} \mathbf{Y}_{m[t,:]}^d \\ [\mathbf{0}]_{p \times 1} \\ \gamma_2 \phi_{[t,:]}^{(iter-1)} + \gamma_3 \phi_{[(t-1),:]} \end{bmatrix}, \quad \text{and} \quad \tilde{\mathbf{M}} = \begin{bmatrix} \mathbf{A}^d \\ \gamma_4(\sqrt{D} - (\mathbf{I}_{p \times p} \circ \sqrt{D})) \\ (\gamma_1 + \gamma_2 + \gamma_3)\mathbf{I}_{p \times p} \end{bmatrix},$$

with all parameters being the same as those defined in Section 3.3 of the main text. Here, $[\mathbf{0}]_{p \times 1} \in \mathbb{R}^p$ represents a column vector of zeros, and $\mathbf{Y}_{m[t,:]}^d \in \mathbb{R}^N$ denotes the measurement in the m -th trial of state d at time t .

12 General Experimental Details

All experiments and code were developed and executed using Python version 3.10.4 and are compatible with standard desktop machines. All data used in the experiments are publicly available, and the corresponding code will be shared on GitHub upon publication.

13 Synthetic Data—Additional Information

13.1 Synthetic Generation Details

We initiated the synthetic data generation process by setting the number of channels to $N = 100$ and the maximum number of BBs to $p = 10$. We further defined the number of states as $D = 3$ and determined the number of time points in each observation to be $T^d = 300$, where d represents the state index (here $d \in \{1, 2, 3\}$). We defined the number of trials for each state as one, i.e., $M_d = 1$ for $d = 1, 2, 3$.

We first initialized a "general" BB matrix (\mathbf{A}) as the initial structure, which will later undergo minor modifications for each state. We determined the number of non-zero values k^j (i.e., the cardinality) for each j -th BB in the general \mathbf{A} matrix by sampling from a uniform distribution between 1 and 21. Next, we sampled the values in each j -th BB from normal distribution (zero mean and unit variance), and set all but the top k_j values to zero. For each state d , we generated the time-traces Φ^d via a linear combination of 15 trigonometric signals, such that the temporal trace of the j -th BB is defined as $\Phi_{:,j}^d = \sum_{i=1}^{15} c_i f_i(\text{freq}_i * x)$ where x is an array of $T = 300$ time points ($x = 1 \dots 300$), freq_i is an array of random frequencies sampled uniformly on $[0, 5]$, f refers to a random choice between the sine and cosine functions (with probability 1/2 for each), and the sign (c_i) was flipped (+1 or -1) with a probability of 1/2.

During the data generation process, we incorporated checks and updates to \mathbf{A} and Φ to ensure that the BBs and their corresponding time traces are neither overly correlated nor orthogonal, are not a simple function of the states labels, and that different BBs exhibit comparable levels of contributions. This iterative process involving the checks persisted until no further modifications were required.

The first check aimed to ensure that the temporal traces of at least two BBs across all states were not strongly correlated with the state label vector ($[1, 2, 3]$) at each time point. Specifically, we examined whether the temporal traces of a j -th BB across all states ($\Phi_{t,j}^1, \Phi_{t,j}^2, \Phi_{t,j}^3$) exhibited high correlation with the state label vector at each time point. This check was important to avoid an oversimplification of the problem by preventing the temporal traces from being solely influenced by the state labels. To perform this check, we calculated the average correlation between the temporal traces and the state labels ($[1, 2, 3]$) at each time point. If the average correlation over time exceeded a predetermined threshold of 0.6, we introduced additional variability in the time traces of the BB that exhibited a high correlation with the labels. This was achieved by adding five randomly generated trigonometric

functions to the corresponding BB. These additional functions were generated in the same manner as the original data (with $\Phi_{:,j}^d = \sum_{i=1}^5 c_i f_i(\text{freq}_i \cdot x)$).

The second check ensured that the time traces were not highly correlated with each other and effectively represented separate functions. If the correlation coefficient between any pair of temporal traces of different BBs within the same state exceeded a threshold of $\rho = 0.6$, the correlated traces were perturbed by adding zero-mean Gaussian noise with a standard deviation of $\sigma = 0.02$.

Next, we ensured that the BBs represented distinct components by verifying that they were not highly correlated with each other. Specifically, if the correlation coefficient between a pair of BBs ($\mathbf{A}_{:,j}, \mathbf{A}_{:,i}$ for $j, i = 1 \dots 10$) within a state exceeded the threshold $\rho = 0.6$, each BB in the highly-correlated pair was randomly permuted to ensure their distinctiveness.

To prevent any hierarchical distinction or disparity in BB contributions and differentiate our approach from order-based methods like PCA or SVD, we evaluated each BB's contribution by measuring the increase in error when exclusively using that BB for reconstruction. Specifically, for the j -th BB of state d , we calculated its contribution as $\text{contribution}_j = -\|\hat{\mathbf{Y}}^d - \mathbf{A}_{:,j}^d \otimes \Phi_{:,j}^d\|_F$, where \otimes denotes the outer product. Then, we compared the contributions between every pair of BBs within the same state. If the contribution difference between any pair of BBs exceeded a predetermined threshold of 10, both BBs in the pair were perturbed with random normal noise. Subsequently, a hard-thresholding operation was applied to ensure that the desired cardinality was maintained.

To introduce slight variability in the BBs' structure across states, the general basis matrix \mathbf{A} underwent modifications for each of the states. In each state and for each BB, a random selection of 0 to 2 non-zero elements from the corresponding BB in the original \mathbf{A} matrix were set to zero, effectively introducing missing channels as differences between states, such that \mathbf{A}^d is the updated \mathbf{A} modified for state d . Finally, the data was reconstructed using $\mathbf{Y}^d = \mathbf{A}^d(\Phi^d)^T$ for each state $d = 1, 2, 3$.

13.2 Experimental details to the Synthetic data

We applied SiBBLInGS to the synthetic data with $p = 10$ components and a maximum number of 10^3 iterations, while in practice about 50 iterations were enough to converge (see Supplementary Fig. 5). The parameters for the λ update in Equation (4) were $\epsilon = 0.01$, $\beta = 0.09$, and $w_{\text{graph}} = 1$. For the regularization of Φ in Equation (6), the parameters used were $\gamma_1 = 0.1$, $\gamma_2 = 0.1$, $\gamma_3 = 0$, and $\gamma_4 = 0.0001$. ν was set to be a vector of ones with length $p = 10$. The number of repeats for the \mathbf{A} update within an iteration, for each state, is $\text{numreps} = 2$. The number of neighbors used in the channel graph reconstruction in Equation (3) is $k = 25$. The python scikit-learn's [44] LASSO solver was used for updating \mathbf{A} in each iteration. This synthetic demonstration used the supervised case for building \mathbf{P} , where \mathbf{P} was defined assuming similar similarity levels between each pair of states, by defining $\mathbf{P} = \mathbf{1} \otimes \mathbf{1}^T \in \mathbb{R}^{3 \times 3}$ (the case described in Supplementary section 9.1.1, with $c = 1$).

13.3 Jaccard index calculation

In Figure 1C, we computed the Jaccard similarity index between the identified BBs by SiBBLInGS and the ground truth BBs. To obtain this measure, we first rearranged the BBs based on the correlation of their temporal traces with the ground truth traces (since the method is invariant to the order of the BBs). Then, we nullified the 15 lower percentiles of the \mathbf{A} matrix, which correspond to values close to zero. Finally, we compared the modified identified BBs to the ground truth BBs using the "jaccard_score" function from the sklearn library [44].

13.4 Extraction of \mathbf{A} and Φ from PARAFAC decomposition

In Figure 1, we utilized the TensorLy python package [33] to perform the PARAFAC decomposition comparison [26] with a rank of p (where $p = 10$ for the synthetic data). The BBs (columns of \mathbf{A}) were defined as the first dimension PARAFAC latent factors, the temporal traces were defined as the second dimension factors, multiplied by the corresponding values from the third dimension to capture the temporal variability over states. To compare to the ground truth, the BBs and temporal traces were reordered based on the temporal traces to maximize the correlation between the PARAFAC traces and ground truth traces. To calculate the Jaccard index for Figure 1E, we kept the k^j highest absolute values from each reordered BB, where k^j represents the number of non-

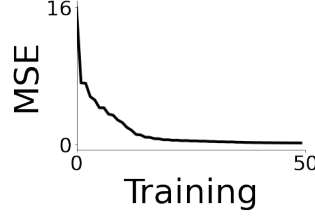


Figure 5: MSE of the model over training iterations for synthetic data.

	CA	FL	IL	LA	MD	MI	NY	WA
BB 1	Berkeley, Campus, College, Harvard, Phd, Princeton	Admissions, Campus, College, Harvard, Phd, Princeton	Admissions, Campus, College, Harvard, Phd, Princeton	Admissions, Campus, College, Harvard, Phd, Princeton	Admissions, Campus, College, Harvard, Phd, Princeton	Admissions, Campus, College, Harvard, Phd, Princeton	Admissions, Berkeley, Campus, College, Harvard, Princeton	Admissions, Campus, College, Harvard, Phd, Princeton
BB 2	Atikomen, Chametz, Charoset, Haggadah, Pesach, Seder	Atikomen, Chametz, Charoset, Haggadah, Passover, Pesach, Seder	Chametz, Charoset, Haggadah, Passover, Pesach, Seder	Chametz, Charoset, Haggadah, Passover, Pesach, Seder	Atikomen, Chametz, Charoset, Haggadah, Passover, Pesach, Seder	Chametz, Charoset, Haggadah, Passover, Pesach, Seder	Atikomen, Chametz, Charoset, Haggadah, Passover, Pesach, Seder	Chametz, Charoset, Haggadah, Passover, Pesach, Seder
BB 3	Auld lang syne, Chicken soup, Decorations, Depression, Gpa, Sweets	Auld lang syne, Champagne, Chicken soup, Decorations, Gpa, Sweets	Auld lang syne, Chicken soup, Decorations, Depression, Gpa, Sweets	Auld lang syne, Champagne, Chicken soup, Decorations, Gpa, Sweets	Auld lang syne, Champagne, Chicken soup, Decorations, Gpa, Sweets	Auld lang syne, Champagne, Chicken soup, Decorations, Gpa, Sweets	Auld lang syne, Champagne, Chicken soup, Countdown, Decorations, Sweets	Auld lang syne, Champagne, Chicken soup, Decorations, Depression, Sweets
BB 4	Elf, Gift, New years eve, Poinsettia, Ugly sweater	Elf, Gift, New years eve, Poinsettia, Ugly sweater	Elf, Gift, New years eve, Poinsettia, Ugly sweater	Elf, Gift, New years eve, Poinsettia, Ugly sweater	Elf, Gift, New years eve, Poinsettia, Ugly sweater	Elf, Gift, New years eve, Poinsettia, Ugly sweater	Elf, Gift, New years eve, Poinsettia, Ugly sweater	Elf, Gift, New years eve, Poinsettia, Ugly sweater
BB 5	Cdc, Hopkins, Kippur, N95, Quarantine, Zoom	Cdc, Hopkins, Mit, N95, Quarantine, Zoom	Cdc, Hopkins, N95, Quarantine, Zoom	Cdc, Hopkins, Mit, N95, Quarantine, Zoom	Cdc, Hopkins, N95, Quarantine, Zoom	Cdc, Hopkins, N95, Quarantine, Zoom	Cdc, Hopkins, N95, Quarantine, Zoom	Cdc, Hopkins, Mit, N95, Quarantine, Zoom

Figure 6: Table of clustered words for the Google Trends experiment

zero entries in that BB in the ground truth data. We set the remaining entries in the BB to zero, effectively sparsifying the BB representation. The Jaccard index was then computed by comparing these PARAFAC BBs to the ground truth BBs using the "jaccard_score" function from the sklearn library [44]. In Figure 1E, the comparison to PARAFAC is depicted. The plot utilizes different colors to represent different states, and the averaging is performed over all BBs.

14 Google Trends—Additional Information

14.1 Trends data acquisition and pre-processing

The acquisition and pre-processing of Google Trends data involved manually downloading the data from April 1, 2010, to November 27, 2022, for each of the selected states: California (CA), Maryland (MD), Michigan (MI), New York (NY), Illinois (IL), Louisiana (LA), Florida (FL), and Washington (WA), directly from the Google Trends platform [22]. The comprehensive list of terms, as clustered according to SiBBInGS, is presented in Supplementary Figure 6. To ensure comprehensive coverage of search patterns, the data was downloaded by examining each query in all capitalization formats, including uppercase, lowercase, and mixed case.

The data (in CSV format) was processed using the 'pandas' library in Python [43, 58] and keeping only the relevant information from January 2011 to October 2022, inclusively. We conducted a verification to ensure the absence of NaN (null) values for each term in every selected state. This step confirmed that no terms or states were inadvertently missed during the data downloading process. To pre-process each term, we implemented a two-step normalization procedure. First, the values within the chosen date range were scaled to a maximum value of 100. This step ensured that the magnitude of each term's fluctuations remained within a consistent range. Next, the values for each term were divided by the sum of values across all dates and then multiplied by 100, resulting in an adjusted scale where the area under the curve for each term equaled 100. This normalization procedure accounted for potential variations in the frequency and magnitude of term occurrences, enabling fair comparisons across different terms. By applying these pre-processing steps, we aimed to mitigate the influence of isolated spikes or localized peaks that could distort the overall patterns and trends observed in the data. Since the focus of this processing was on assessing the relative contribution of a term within a BB rather than comparing the overall amplitude and mean of the term across states, factors such as population size and other characteristics of each state were not taken into consideration.

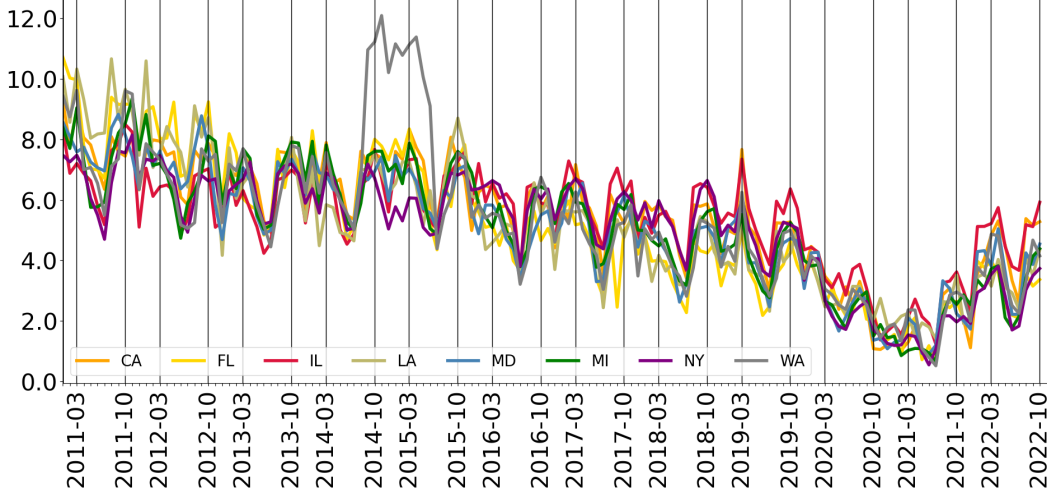


Figure 7: Temporal traces of college admission patterns showing bi-yearly peaks around March and October, aligning with key milestones in the US college admissions process. Additionally, a decrease in online interest in the college BB is observed during the COVID-19 pandemic.

14.2 Experimental details for Google trends

We ran the Trends experiment with $p = 5$ BBs, and applied non-negativity constraints to both the BB components and their temporal traces. The λ 's parameters in Equation (4) included $\epsilon = 9.2$, $\beta = 0.01$, and $w_{\text{graph}} = 35$. For the regularization of Φ in Equation (6), we used the parameters $\gamma_1 = 0$, $\gamma_2 = 0$, $\gamma_3 = 0.05$, $\gamma_4 = 0.55$. The trends example used the data-driven version for studying P , and we set ν to be a vector of ones with length $p = 5$.

During each iteration, A underwent two updates within each state. The number of neighbors we used in the channel graph reconstruction in Equation (3) was $k = 4$. We used the PyLops package in Python, along with the SPGL1 solver [47] to update A in each iteration. With respect to SPGL1 parameters (as described in [47]), we set the initial value of the parameter τ to 0.12, and a multiplicative decay factor of 0.999 was applied to it at each iteration. We note here that SPGL1 solves a Lagrangian variation of the original Lasso problem, where, i.e., it bounds the ℓ_1 norm of the selected BB to be smaller than τ , rather than adding the ℓ_1 regularization to the cost [55, 47].

14.3 Temporal traces of college BB

The temporal traces of the college admission identified BB exhibit distinct bi-yearly peaks, with notable increases in activity around March and October, along with a clear decrease between March to next October (Supplementary Fig. 7). These peaks align with key periods in the college admissions cycle, including application submission and admission decision releases. Particularly, around the end of March, many colleges and universities release their regular admission decisions, prompting increased population interest. Similarly, October marks the time when prospective students typically start showing increased interest in applying to colleges as many colleges have early application deadlines that fall in late October or early November. The bi-yearly peaks pattern in March and October thus reflects the concentrated periods of activity and anticipation within the college admissions process. External factors such as the COVID-19 pandemic can also influence the timing and dynamics of the college admissions process, as we observe by the decrease in the college BB activity during the pandemic period (Supplementary Fig. 7).

14.4 Temporal traces of Passover BB

SiBBInGS identified a “Passover” BB, characterized by temporal traces that show a clear alignment with the timing of Passover, which usually occurs around April. The time traces demonstrate a prominent peak in states with higher Jewish population percentages, like CA, FL, and NY (Supple-

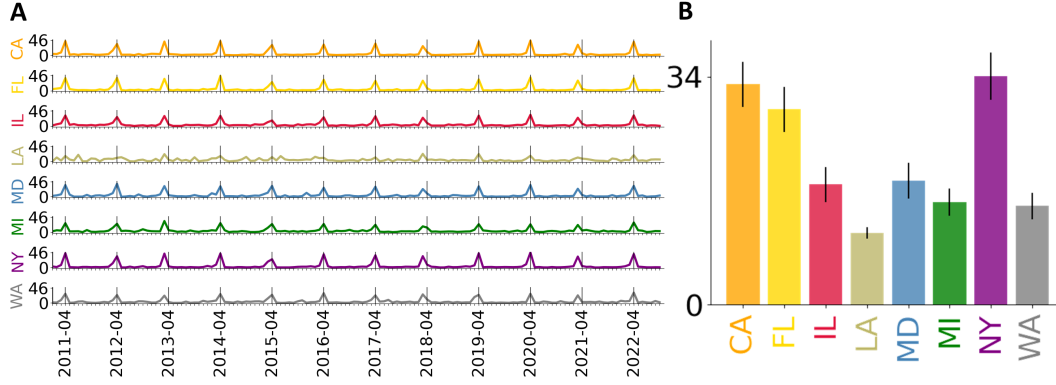


Figure 8: **Temporal trace of Passover BB.** The Passover BB patterns show an alignment with the percentage of Jewish population in different states. **A** Temporal traces of the Passover BB for each state. Vertical black lines indicate the month of April, when Passover is usually celebrated. **B** The mean and standard error of peak values for each state.

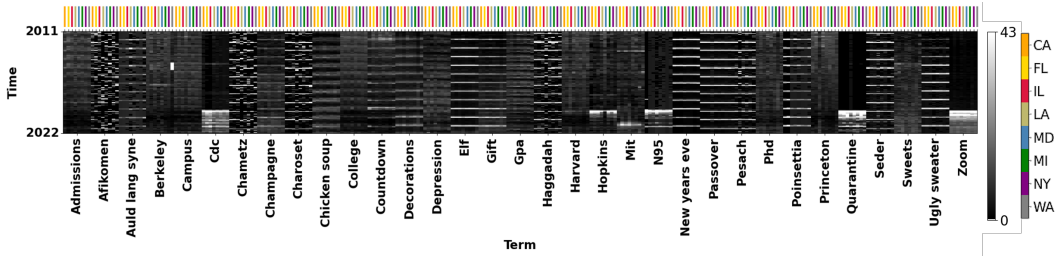


Figure 9: Post-processed data of the temporal activity of the chosen queries, ordered by state and alphabetical order of the queries. The states are marked by the small colorful vertical lines that appear at the top.

mentary Fig. 8), as computed by the average peak value plotted for the different states. The peak finding was done using scipy’s [56] “find_peaks” function with a threshold of 4.

15 Neural Data—Additional Information

15.1 Neural Data Pre-Processing

In this experiment we used the neural data collected from Brodmann’s area 2 of the somatosensory cortex in a monkey performing a reaching-out movement experiment from Chowdhury et al. [14, 15]. While the original dataset includes data both under perturbed and unperturbed conditions, here, for simplicity, we used only unperturbed trials. We followed the processing instructions provided by Neural Latents Benchmark [45] to extract the neural information and align the trials. The original neural data consisted of spike indicators per neuron, which were further processed to approximate spike rates by convolving them with a 60-point wide kernel.

For each of the 8 angles, we randomly selected 18 trials, resulting in a total of 144 data matrices. The states were defined as the angles, and for learning the supervised P , we used as labels the x-y coordinates of each angle in a circle with a radius of 1 (i.e., sine and cosine projections).

15.2 Experimental details for the neural data experiment

We ran SiBBLInGS on the reaching-out dataset with $p = 4$ BBs. The λ ’s parameters used were $\epsilon = 2.1$, $\beta = 0.03$, and $w_{\text{graph}} = 10.1$. For the regularization of Φ we used: $\gamma_1 = 0.001$, $\gamma_2 = 0.001$, $\gamma_3 = 0.1$, and $\gamma_4 = 0.3$ and we set ν to be a vector of length $p = 4$ with $\nu_1 = 0.8$ (to allow more flexibility in the first BB), and $\nu_k = 1$ for $k = 2, 3, 4$. For the neural data, we used the supervised version of P , where the $x - y$ coordinates are used as the labels for calculating P (see Eq. (1)).

During each iteration, \mathbf{A} underwent two updates within each state. We chose $k = 7$ neighbors for the channel graph reconstruction, and used Python scikit-learn’s [44] LASSO solver for the update of \mathbf{A} .

15.3 State prediction using temporal traces

We used the identified temporal traces Φ to predict the state (hand direction). The dimensionality of each state’s temporal activity Φ^d was reduced to a vector of length $p \times 4 = 16$ using PCA with 4 components. A k -fold cross-validation classification approach with $k = 4$ folds was employed. In each iteration, a multi-class logistic regression model with multinomial loss was trained on 3 folds and used to predict the labels of the remaining fold. This process was repeated for each fold, and the results were averaged. The confusion matrix and accuracy scores for each state (angle), as shown in Figure 4C and in Supplementary Figure 10F.

15.4 Computation of $\rho_{\text{within/between}}$

To compute the correlation for the ”within” state case, a random bootstrap approach was employed. Specifically, for each state, we randomly selected 100 combinations of temporal trace pairs corresponding to the same BB but from different random trials within the state, computed the correlations between these temporal trace pairs, and averaged the result over all 100 bootstrapped samples to obtain the average correlation. Similarly, for the ”between” states case, we repeated this procedure with the difference that we selected 100 random bootstrapped combinations of pairs of the same BB but from trials of different states. In Supplementary Figure 10C, the average correlations are shown for each BB. The ratio depicted in Figure 4E represents the ratio between the averages of the ”within” and ”between” state correlations.

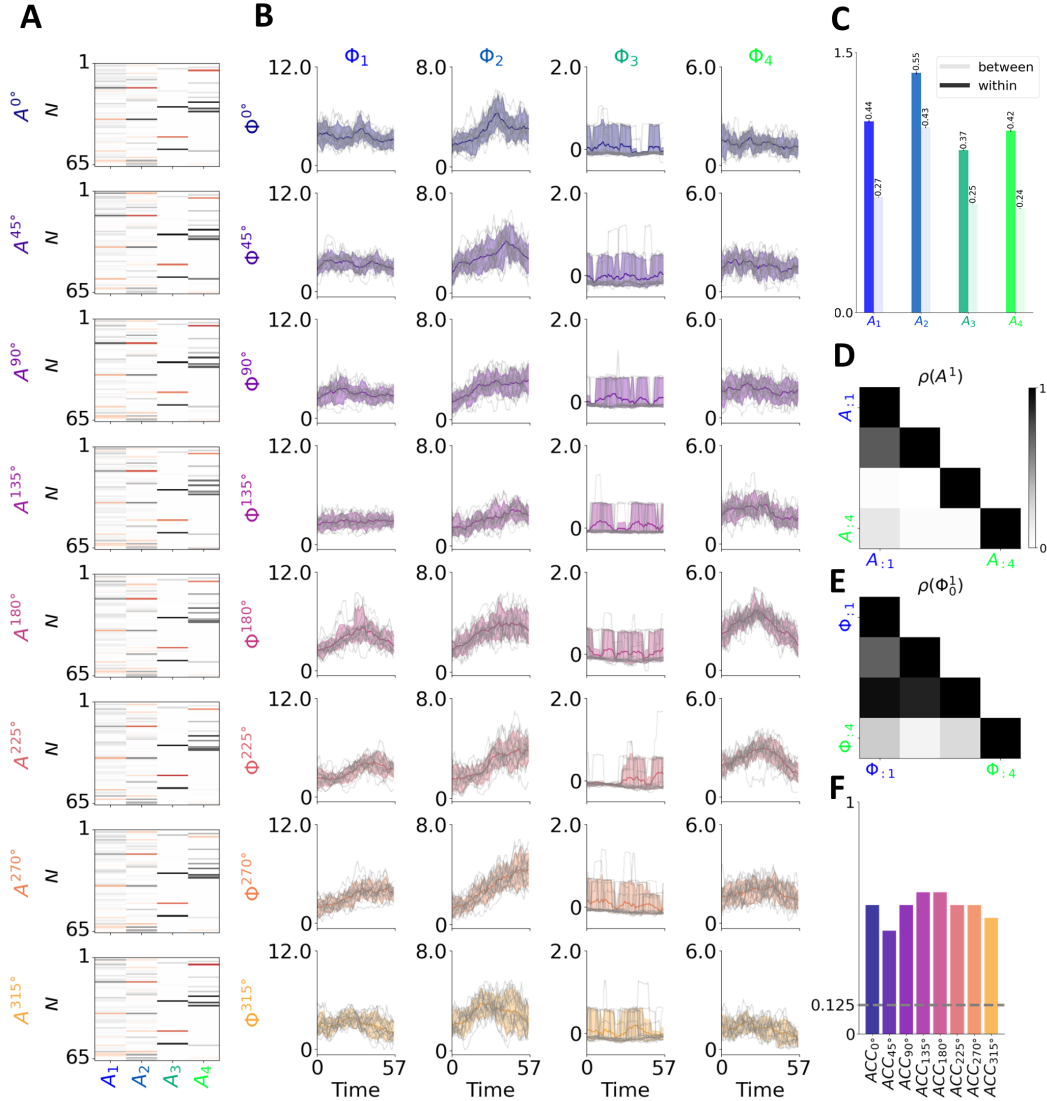


Figure 10: **Additional Figures for the Neural Recordings Experiment.** **A** The identified BBs for the different states. While there is clear consistency, slight modifications can be observed across states, capturing the natural variability in neural ensembles corresponding to different tasks. **B** Temporal traces of the identified BBs, shown with a 90% confidence interval (background color), and all trials are plotted in light gray. The color corresponds to the state color used in Figure 4. We observe adaptation over the states as well as differences between the temporal traces of BBs within a given state. The third BB exhibits significantly lower activity compared to the others (see also Figure 4), suggesting that it might capture general background trends or noise. **C** Within and between temporal trace correlations (averaged over 100 bootstrapped examples) with standard error, colored according to the BB color, and transparency representing the strength of the between (opaque) and within (less opaque) correlations. **D** Example of the correlations between each pair of BBs within the 1-st state (0°). This shows that while some BBs are orthogonal, others are not. **E** Example of within-state correlations between each pair of temporal traces of the BBs within the 1-st trial of the 1-st state (0°), showing that the temporal traces are neither orthogonal nor overly correlated. **F** Accuracy in predicting the state using only the temporal traces of that state as input (colored by the state color). While the random accuracy would be $1/\text{length}(\text{labels}) = \frac{1}{8} = 0.125$, the achieved accuracies are significantly higher for all states.